





RESEARCH ARTICLE | NOVEMBER 01 2023

Effect of pressure on slip length of supercritical water flow in graphene nanochannels

Ming Dong (董明) ; Jinliang Xu (徐进良)  ; Yan Wang (王艳) 



Physics of Fluids 35, 112003 (2023)

<https://doi.org/10.1063/5.0171313>



Articles You May Be Interested In

Hydrodynamic slip of alkali chloride solutions in uncharged graphene nanochannels

J. Chem. Phys. (January 2022)

Slip flow in graphene nanochannels

J. Chem. Phys. (October 2011)

Imbibition dynamics and steady flows in graphene nanochannels with sparse geometric and chemical defects

Physics of Fluids (November 2022)



Physics of Fluids

Special Topics Open
for Submissions

[Learn More](#)



Effect of pressure on slip length of supercritical water flow in graphene nanochannels

Cite as: Phys. Fluids **35**, 112003 (2023); doi: [10.1063/5.0171313](https://doi.org/10.1063/5.0171313)

Submitted: 8 August 2023 · Accepted: 10 October 2023 ·

Published Online: 1 November 2023



View Online



Export Citation



CrossMark

Ming Dong (董明),¹ Jinliang Xu (徐进良),^{1,2,a)} and Yan Wang (王艳)³

AFFILIATIONS

¹Beijing Key Laboratory of Multiphase Flow and Heat Transfer for Low Grade Energy Utilization, North China Electric Power University, Beijing 102206, China

²Key Laboratory of Power Station Energy Transfer Conversion and System, North China Electric Power University, Ministry of Education, Beijing 102206, China

³Beijing Huairou Laboratory, Beijing 101400, China

^{a)} Author to whom correspondence should be addressed: xjl@ncepu.edu.cn

ABSTRACT

Flow transport of supercritical fluids (SFs) in nanopores widely occurs in shale and deep geothermal systems. Pressure is an important parameter for describing SFs, but the effect of pressure on the flow and slip behaviors of SFs in nanochannels is unknown. In this study, molecular dynamics simulations of the Poiseuille flow of supercritical water (SCW) in graphene nanochannels are performed by applying a driving force to water molecules between two walls. Fluid pressure is realized by varying water density. The effect of pressure on the slip length under different surface wettability is investigated. The results show that the slip length nonmonotonically varies with the pressure, which is divided into three regions according to the three-regime-model of SFs. For the gas phase and gas-like SCW, the slip length gradually decreases with increasing pressure. For two-phase-like SCW, the slip length increases with pressure. For liquid-like (LL) SCW, the slip length decreases with increasing pressure. The slip length nonmonotonically varies due to the nonlinear variation of the fluid viscosity and interfacial friction with pressure. For LL SCW, the slip length is linearly related to the inverse of the density ratio, and the effect of pressure and wettability on the slip length is evaluated using the density ratio and energy barrier. Furthermore, the relationship between the slip length and pressure is verified for application to a wide range of wettability, different channel heights, and different fluid types and solid wall types. This study deepens the understanding of the microscale flow theory under supercritical conditions.

Published under an exclusive license by AIP Publishing. <https://doi.org/10.1063/5.0171313>

I. INTRODUCTION

Supercritical fluids (SFs) have attracted extensive attention since they were first discovered. In the fields of shale gas extraction, supercritical geothermal systems, and carbon sequestration, the flow transport of SFs in micropores and nanopores is widespread.^{1–6} For example, supercritical methane undergoes diffusion and adsorption in nanopores during shale gas extraction. Supercritical carbon dioxide (CO₂) adsorbs and flows in shale pores during supercritical hydraulic fracturing. Supercritical CO₂ undergoes flow and heat transfer in hot dry rock pores. The system efficiency is largely determined by the nature and behavior of SFs in nanopores. However, the flow behavior of SFs in the nanoscopic scale is still unclear compared to that in the macroscopic scale,^{7–9} which severely limits the application of SFs.

Fluid flow transport in nanochannels has received attention due to the rapid development of nanotechnology and has gradually become a hot topic in the fields of micro-electromechanical systems, drug

transport, and membrane separation.^{10–12} At the microscopic scale, the reduction in the characteristic scale of flow results in the no-slip boundary condition at the macroscopic scale no longer being applicable.^{13,14} The flow at the nanoscale exhibits interfacial slip behavior, which stems from the relative motion of the near-wall fluid. Usually, the slip length (L_s) is used to quantitatively characterize the slip behavior.¹³ During the past 20 years, researchers have investigated the interfacial slip behavior, focusing on the effects of fluid–solid interactions,^{15,16} gas layer,^{17–19} shear rate,²⁰ wall roughness,^{21,22} and channel size^{23–25} on the slip length. However, the above environmental conditions have mainly focused on ambient temperature and pressure, where the fluid is in the subcritical liquid or gas state. During shale gas extraction, the reservoir environment has high temperature and pressure conditions,⁷ where the fluid is in the supercritical state.

Studies on the flow transport of SFs have mainly focused on shale gas extraction. For example, Zhan *et al.*²⁶ and Shan *et al.*²⁷ investigated

the flow behavior of methane in inorganic and organic nanopores via molecular dynamics (MD) simulations. They found that velocity exhibits a parabolic distribution in inorganic nanopores, while it exhibits a plug-like distribution in organic nanopores. Wang *et al.*²⁸ obtained similar results in the simulation of supercritical CO₂ flow in graphene slits. Graphene slits showed a visible velocity slip, which greatly reduced the flow resistance and improved the gas transport efficiency. In addition, the slip length gradually decreased with increasing temperature and pore size. He *et al.*²⁹ reported the effect of wall roughness on the supercritical methane flow in graphene nanopores. They found that the slip velocity of a rough wall was lower than that of a smooth wall and that the effect of roughness was related to the pore size. Huang *et al.*³⁰ constructed realistic kerogen nanopores with different roughness by MD. The results showed that the resistance increased with the roughness, leading to a decrease in the flow rate. Sidorenkov *et al.*³¹ investigated the effect of pore shape on methane flow in graphene nanopores. Their simulation showed that the pore shape had a slight effect on the slip velocity. The velocity distribution in circular nanopores is consistent with the prediction of the classical Poiseuille flow. Assuming that water was originally present in the shale reservoir and was introduced during hydraulic fracturing, Liu *et al.*³² simulated the two-phase flow of methane and water in hydroxyl silica nanopores. They found that water forms hydrogen bonds with the hydroxyl groups of walls, yielding an adsorbed water film near the nanopores. As the pressure increased, the water film near the walls interconnected and formed water bridges in the channel, leading to a gradual decrease in methane flow. MD simulations of methane–water mixtures by Wang *et al.*³³ also revealed that water molecules adsorbed on the wall surface and formed a water film in inorganic nanopores, while water molecules agglomerated in the center of the channel and formed clusters in graphene nanopores. Zhang *et al.*³⁴ investigated the effect of water content on the flow behavior of methane/CO₂–water in organic nanopores. They found that the slip length of methane/CO₂ was almost constant for water content below 50% and significantly decreased with increasing water content.

In summary, the studies on the flow transport of SFs in shale fields have focused on the effects of wall type, wall roughness, pore size, and fluid components. Although pressure is an important parameter for describing SFs, there are relatively few studies on the effect of pressure on flow. The effect of pressure on the slip length is still unclear.^{35–38} Liang and Koblinski³⁵ reported different patterns of slip length with variable pressure for supercritical argon on graphene and gold surfaces. The slip length on the graphene surface first decreased and then increased with increasing pressure. In contrast, the slip length on gold surface monotonically decreased with increasing pressure. Furthermore, Shan *et al.*³⁶ reported that the slip length nonmonotonically varied with pressure (density) for supercritical argon on the graphene surface based on the molecular kinetic theory and MD simulation. The slip length first decreased and then increased with increasing pressure, and the slip length minimum can be explained by competing fluid–solid and fluid–fluid molecular interactions. The MD results of Nan *et al.*³⁷ show that the slip length of supercritical methane on the graphene surface both monotonically and nonmonotonically varies with pressure, depending on the fluid temperature. For fluid temperature below 350 K, the slip length first decreased and then slowly increased with increasing pressure. For fluid temperature above 400 K, the slip length monotonically decreased with increasing

pressure. Barrat and Bocquet³⁸ reported that the effect of pressure on the slip length of Lennard–Jones (LJ) fluids on solid walls with face-centered cubic (FCC) lattice is related to surface wettability. The slip length monotonically decreased with increasing pressure under weak wettability, while it was almost unaffected by pressure under strong wettability.

The effect of pressure on the slip length could be related to the type of solid wall (graphene and metal), the type of SFs workpiece (LJ fluid and methane), and the surface wettability. The above issues are important because the flow slip strongly influences the flow resistance and system efficiency for SFs. However, such a problem is complex and still controversial. The effects of pressure and surface wettability on the slip length need to be revealed. In this study, water is chosen as the fluid workpiece, which is the most widely used fluid at supercritical pressure and can be compared with LJ fluids and methane for analyzing the effect of the type of SFs workpiece. In addition, two solid wall materials, graphene and metallic copper, are used to analyze the effect of the type of solid walls. This study aims to investigate the effect of pressure on the slip length of SFs under different wettability.

This study investigates the Poiseuille flow of supercritical water (SCW) in graphene and metallic copper nanochannels by MD simulation. The effect of pressure on the slip length under different surface wettability is analyzed. The structure of the paper is arranged as follows: Section II provides the details of the MD simulation and analysis methods of relevant parameters. Section III presents the results and discussion, which is divided into four subsections. Section III A reports the effect of pressure on the velocity distribution of SCW in graphene nanochannels, showing that the nonmonotonic variation of velocity distribution with increasing pressure stems from the variation of intermolecular interaction forces with pressure. Sections III B and III C focus on the effect of pressure on the slip length under different surface wettability and present the explanation based on the interface friction perspective for the variation of the slip length with increasing pressure: the slip length first decreases, then increases, and finally decreases with increasing pressure. The density ratio (ρ_f/ρ_a) and the energy barrier ($\Delta E/\epsilon_f$) parameters are proposed to effectively describe the influence of pressure and wettability. Section III D further verifies the relationship between the slip length and pressure under a wide range of wettability, channel height, type of solid walls, and fluid workpiece. The paper is summarized in Sec. IV. The results highlight the microscale flow slip theory at high temperatures and pressures and provide theoretical guidance for SFs flow, such as shale gas.

II. SIMULATION AND METHODS

A. Poiseuille flow

Figure 1(a) shows the physical model of the Poiseuille flow of water in the graphene nanochannel. The system contains top and bottom solid walls, with water molecules in between them. The simulated system size is $L_x \times L_y \times L_z = 4.68 \times 4.68 \times 8.6 \text{ nm}^3$. The channel height (H) between the two solid walls is 5.0 nm. The periodic boundary condition is applied along the x - and y -directions, and the fixed boundary condition is applied along the z -direction. The two solid walls contain six layers of graphene with each spacing of 0.335 nm. The bond length between the adjacent carbon atoms is 0.142 nm. In the simulation, different pressure values are obtained by varying the water density (the number of water molecules).

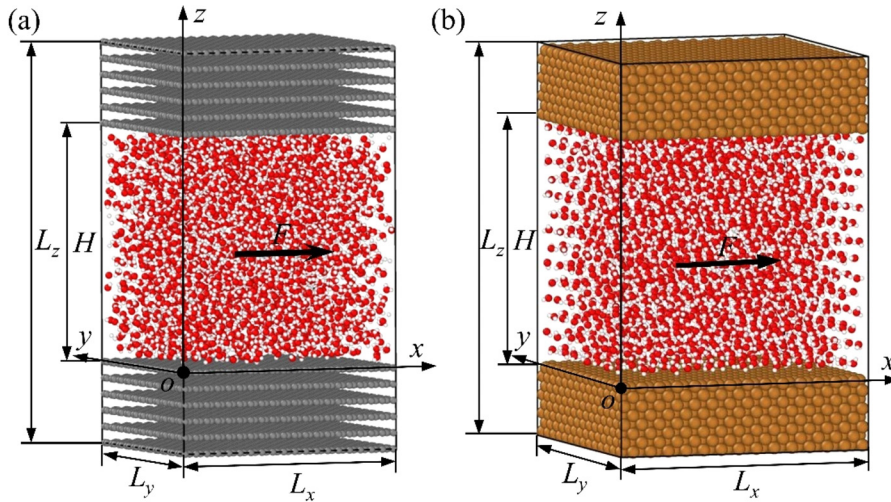


FIG. 1. Physical model of the Poiseuille flow of SCW: (a) graphene nanochannel with the system size $L_x \times L_y \times L_z = 4.68 \times 4.68 \times 8.6 \text{ nm}^3$ and channel height $H = 5.0 \text{ nm}$ and (b) copper nanochannels with system size $L_x \times L_y \times L_z = 5.06 \times 5.06 \times 8.0 \text{ nm}^3$ and channel height $H = 5.0 \text{ nm}$.

The TIP4P/2005 model is used for water molecules, which not only reproduces the surface tension of water but also accurately describes the phase diagram position.^{39–41} TIP4P/2005 model comprises the LJ potential energy and the Coulomb potential energy, and is written as⁴⁰

$$\phi(r_{ij}) = 4\epsilon \left[\left(\frac{\sigma}{r_{ij}} \right)^{12} - \left(\frac{\sigma}{r_{ij}} \right)^6 \right] + \frac{q_i q_j}{4\pi\epsilon_0 r_{ij}}, \quad (1)$$

where ϵ is the energy parameter, representing the potential well depth, σ is the size parameter, r is the distance between atoms i and j , q is the charge, and ϵ_0 is the vacuum dielectric constant. The TIP4P/2005 model is a four-point rigid-body model, including one oxygen atom, two hydrogen atoms, and one virtual atom point. The oxygen atom considers both LJ potential energy and Coulomb potential energy, and the hydrogen atom considers only the Coulomb potential energy. The bond length (l_{OH}) and bond angle (θ_{HOH}) of the water molecule are kept constant due to the rigid-body model. The parameters values are as follows:⁴⁰ $\sigma_{\text{O}} = 0.31589 \text{ nm}$, $\epsilon_{\text{O}} = 0.00803 \text{ eV}$, $l_{\text{OH}} = 0.09572 \text{ nm}$, $\theta_{\text{HOH}} = 104.52^\circ$, $q_{\text{O}} = -1.128 \text{ e}$, and $q_{\text{H}} = 0.5564 \text{ e}$.

The interaction of in-plane carbon atoms of graphene is usually described by the Tersoff potential,⁴² and the interaction of interplanar carbon atoms between different graphene layers is usually described by the LJ potential.⁴³ For the flow of water on the graphene surface, the choice of flexible or rigid walls slightly affects the slip length.^{44,45} The objective of the study is to investigate the effect of pressure on the slip length. Therefore, rigid graphene walls are used to save computational resources.⁴⁶ Surface wettability is determined by the interaction energy between fluid and solid molecules. Here, wettability is described through the LJ interaction between the oxygen atoms of water and carbon atoms of graphene,^{39,46}

$$\phi(r_{ij}) = 4\epsilon_{\text{C-O}} \left[\left(\frac{\sigma_{\text{C-O}}}{r_{ij}} \right)^{12} - \left(\frac{\sigma_{\text{C-O}}}{r_{ij}} \right)^6 \right], \quad (2)$$

where $\sigma_{\text{C-O}}$ and $\epsilon_{\text{C-O}}$ are size and energy parameters, respectively. The value of $\sigma_{\text{C-O}}$ is 0.319 nm , which is also used in the literature.⁴⁶ Wettability is adjusted by varying the value of $\epsilon_{\text{C-O}}$.

The Newton equation is written as⁴⁷

$$m \frac{d^2 \vec{r}_{ij}}{dt^2} = \sum_{j \neq i, j=1} \vec{F}_{ij} + \vec{F}_{\text{ex}}, \quad (3)$$

where m is the atomic mass, F_{ij} is the force between two atoms, and F_{ex} is the external force. An external force is applied for each water molecule to realize Poiseuille flow. The Velocity-Verlet algorithm is used to solve the Newtonian equations. The position, acceleration, and velocity information at moment t are known. Thus, the position $r(t+\Delta t)$, acceleration $a(t+\Delta t)$, and velocity $v(t+\Delta t)$ at moment $t+\Delta t$ are⁴⁷

$$r(t+\Delta t) = r(t) + v(t)\Delta t + \frac{1}{2}a(t)\Delta t^2, \quad (4)$$

$$v(t+\Delta t) = v(t) + \frac{1}{2}[a(t) + a(t+\Delta t)]\Delta t, \quad (5)$$

where $\Delta t = 1 \text{ fs}$ is the timescale. In the simulation, the cutoff distance for both LJ and Coulomb potentials is 1.5 nm .⁴⁸ The long-range Coulomb force of the water molecule is calculated by the PPPM algorithm,⁴⁹ and the rigid water molecule is fixed by the SHAKE algorithm.⁵⁰ After energy minimization, equilibrium molecular dynamics simulations are first performed with a Nose-Hoover⁵¹ heat bath, and the fluid is maintained at a constant system temperature (660 K) under the NVT ensemble. After the relaxation of 5 ns , non-equilibrium molecular dynamics simulations are performed to realize Poiseuille flow by applying an external force ($0.5 \times 10^{-4} \text{ eV/nm}$), which is within the force range chosen by Wagemann *et al.*⁵² For temperature calculations, the center-of-mass velocity of the fluid should be excluded and only the velocity of thermal motion is employed. A biased Nose-Hoover thermostat without the center-of-mass velocity is applied to control the fluid temperature.^{53,54} The system relaxation is continued for 10 ns to reach the equilibrium state and ensure that the velocity distribution does not significantly change. Finally, a run of 4 ns is performed to obtain the statistical average of the physical parameters. The open-source software LAMMPS (Large-scale Atomic/Molecular Massively Parallel Simulator) is used for simulation.⁵⁵

In addition to the graphene nanochannel, the Poiseuille flow of water in a metallic copper nanochannel is also simulated. The simulated

system size is $L_x \times L_y \times L_z = 5.06 \times 5.06 \times 8.0 \text{ nm}^3$ [see Fig. 1(b)]. The channel height (H) between the copper nanochannels is 5.0 nm, which is consistent for graphene nanochannels. The copper wall is filled with eight layers of copper atoms and arranged in an FCC lattice (lattice constant is 0.3615 nm) with (100) crystal faces in contact with the fluid. The simulation parameters are the same as those for the graphene system.

B. Surface wettability

The contact angle (θ_c) is used to characterize the surface wettability under subcritical pressure. In the study, the water-graphene wetting process is simulated by MD to obtain the relationship between the contact angle and the fluid-solid interaction (ϵ). The SPC/E model has been used in most studies on water-graphene wetting simulation,^{46,56} but it does not accurately describe the physical properties of SCW compared to the TIP4P/2005 model.⁴¹ A few MD simulations using the TIP4P/2005 model,³⁹ the parameters, such as the number of graphene layers and cutoff distance, are different from those used in this study. Therefore, instead of directly adopting the interaction parameters in the literature, this study simulates the wetting of the TIP4P/2005 model water on the six-layer graphene surface, which is consistent for model setup under Poiseuille flow. Figure 2(a) shows the physical model of the wetting process for water on the graphene surface. The system size is $L_x \times L_y \times L_z = 23.8 \times 2.72 \times 12.2 \text{ nm}^3$. The bottom of the system is filled with six layers of graphene, and cylindrical water with a diameter of 6 nm is filled above the wall. The water density is 997 kg/m^3 under 300 K and 0.1 MPa conditions. A Nose-Hoover⁵¹ heat bath is used to maintain the system temperature at 300 K. The rest of the simulation parameters are the same as those for the Poiseuille flow simulation. A 6 ns relaxation is first run to reach equilibrium, followed by 2 ns run to obtain the wetting interface. The contact angle can be obtained by circular fitting of the droplet gas-liquid interface. Here, the $0.5(\rho_l + \rho_v)$ density line is considered as the gas-liquid interface contour, where ρ_l and ρ_v are the liquid and gas densities, respectively.

In early studies, for the contact angle of water on the graphene surface, it was usually assumed that graphene has similar hydrophobic properties as graphite with a contact angle of 80° .⁵⁷ However, with the advancement of graphene preparation and transfer techniques, the contact angles of water-graphene have been explored in the range of 30° – 120° .^{58–60} Such a large range of contact angles depends on the substrate properties, number of graphene layers, surface roughness, cleanliness, and measurement methods.^{61–63} In this study, three typical contact angles of 50° , 80° , and 110° are selected, corresponding to three typical surface wettability conditions: hydrophilic, medium, and hydrophobic, respectively. The parameter $\sigma_{C-O} = 3.19 \text{ \AA}$ is fixed, and ϵ_{C-O} (0.002–0.006 eV) is adjusted to obtain the relationship between θ_c and ϵ_{C-O} . Figure 2(b) shows the variation of θ_c with ϵ_{C-O} . The void circles represent the relationship of the θ_c and ϵ_{C-O} based on the results of wetting simulations. The corresponding ϵ_{C-O} for the three typical wettability ($\theta_c = 50^\circ$, 80° , and 110°) are 0.005 72, 0.004 32, and 0.002 88 eV, respectively.

For the contact angle of water on the metallic copper surface, the above wetting model is also adopted. The parameters ϵ_{Cu} and σ_{Cu} are 0.4095 eV and 0.2338 nm, respectively. The contact angle is calculated by fixing $\sigma_{Cu-O} = (\sigma_{Cu} + \sigma_O)/2 = 0.275 \text{ nm}$. Figure 2(c) shows the relationship between θ_c and ϵ_{Cu-O} .

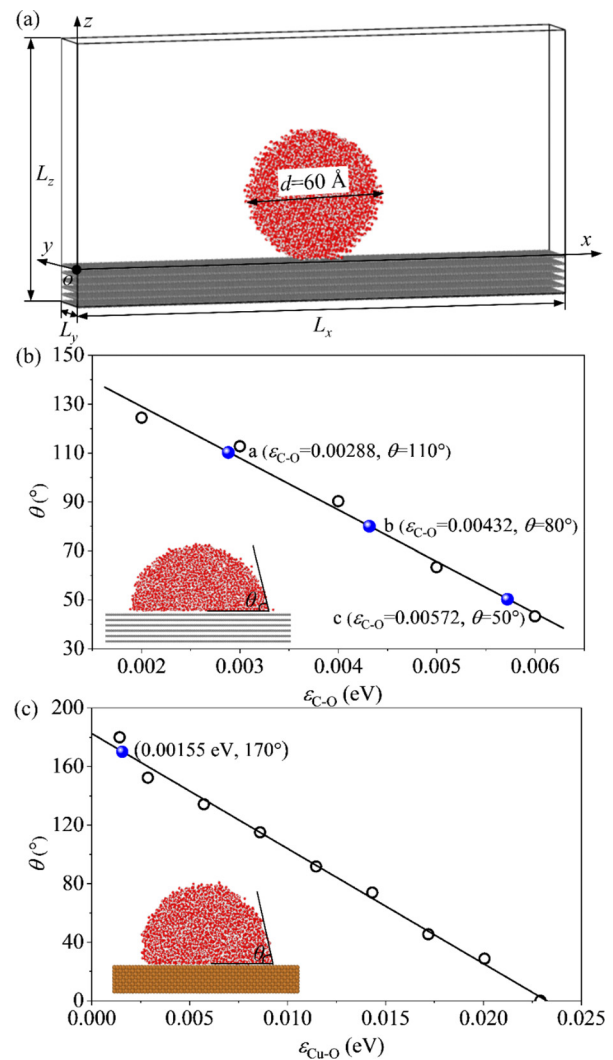


FIG. 2. Relationship between the contact angle (θ_c) and the flow-solid interaction (ϵ_{C-O}): (a) physical model of the water wetting, (b) θ_c vs ϵ_{C-O} in graphene nanochannel, in which $\theta_c = 50^\circ$, 80° , and 110° at $\epsilon_{C-O} = 0.005 72$, $0.004 32$, and $0.002 88$ eV, respectively, and (c) θ_c vs ϵ_{Cu-O} in copper nanochannel, in which $\theta_c = 170^\circ$ at $\epsilon_{Cu-O} = 0.001 55$ eV.

C. Slip length

The slip length is usually calculated using the slip model proposed by Navier,¹⁵ $L_s = u_s/\gamma$, where L_s is the interfacial slip length, u_s is the slip velocity, and γ is the interfacial shear rate, $\gamma = \partial u/\partial n$. The velocity distribution of water on the graphene surface is plug flow. If the slip length is directly calculated based on the epitaxial velocity distribution profile, small changes in the velocity distribution at the fluid-solid interface will result in a large statistical error.⁶⁴ Here, the slip length is determined as follows. According to the linear momentum conservation in the flow direction, the wall shear force (τ_w) is equal to the total force applied to the fluid, $\tau_w = fH/2$. Combined with the equation $\tau_w = \eta du/dz$ for Newtonian fluids, the slip length can be expressed as⁶⁵

04 November 2024 09:30:57

$$L_s = \frac{2\eta u_s}{fH} = \frac{2\eta \bar{u}}{fH}, \quad (6)$$

where \bar{u} is the mean fluid velocity, η is the shear viscosity, and f is the volume force. Compared to the mean velocity, the slip velocity at the fluid–solid interfaces lightly fluctuates during the statistical averaging (see Fig. 4). The velocity distribution of SCW on the graphene wall is plug flow. Therefore, using the mean velocity to reduce the statistical error of the slip velocity is reasonable.⁶⁵

D. Fluid pressure

In the study, fluid pressure is varied by changing the water density in the nanochannel. In a confined space, the attraction of solid wall to fluid molecules causes density stratification (density oscillation) of the near-wall fluid, resulting in pressure oscillation.^{66,67} If the average pressure of the fluid in the whole nanochannel is used as fluid pressure, the pressure oscillation behavior will cause the pressure to deviate from the set pressure. Pham *et al.*⁶⁸ found that the pressure at the fluid–solid interface is difficult to define. However, in the central region away from the wall, the fluid density and pressure do not oscillate, so the average pressure in this region is used as the fluid pressure. Here, the average pressure $S = (S_{xx} + S_{yy} + S_{zz})/3$ in the central region (1–4 nm) away from the wall is used as the fluid pressure. The pressure tensor ($S_{\alpha\beta}$) is calculated as⁶⁹

$$S_{\alpha\beta} = -mv_\alpha v_\beta - W_{\alpha\beta}, \quad (7)$$

where the first term is the kinetic energy contribution from atoms, v_α and v_β are the velocity components in the direction of α and β , respectively, and the second term $W_{\alpha\beta}$ is the virial contribution from the intramolecular- and intermolecular interactions. For the water molecule, the virial term can be further written as⁶⁹

$$\begin{aligned} W_{\alpha\beta} = & \frac{1}{2} \sum_{n=1}^{N_p} (r_{1\alpha} F_{1\beta} + r_{2\alpha} F_{2\beta}) + \frac{1}{2} \sum_{n=1}^{N_b} (r_{1\alpha} F_{1\beta} + r_{2\alpha} F_{2\beta}) \\ & + \frac{1}{3} \sum_{n=1}^{N_a} (r_{1\alpha} F_{1\beta} + r_{2\alpha} F_{2\beta} + r_{3\alpha} F_{3\beta}) \\ & + K_{\text{space}}(r_{1\alpha}, F_{1\beta}) + \sum_{n=1}^{N_f} r_{1\alpha} F_{1\beta}, \end{aligned} \quad (8)$$

where the first term presents the contribution of pairwise interactions, $r_{1\alpha}$ and $r_{2\alpha}$ are the positions of two atoms in pairwise interactions, $F_{1\alpha}$ and $F_{2\alpha}$ are the forces of the two atoms in pairwise interactions, N_p is the neighboring atoms around each atom, the second and third terms are the contributions of the bond and angle of the water molecule, respectively, the fourth term represents the contribution of long-range Coulombic interactions, and the fifth term represents the contribution of internal constraint forces.

E. Interfacial friction coefficient

The interfacial friction coefficient (κ) for a low shear flow can be calculated using the Green–Kubo relationship,⁶⁴

$$\kappa = \frac{1}{Ak_B T} \int_0^\infty \langle F_x(t) F_x(0) \rangle dt, \quad (9)$$

where F_x is the force of the solid wall on the fluid molecules in the flow direction (x -direction), A is the surface area, k_B is the Boltzmann

constant, and T is the system temperature. Note that κ needs to be obtained in the equilibrium molecular dynamics simulation stage.

F. Three-regime-model of SCW

Experiments and MD simulations have shown the heterogeneous structure of SFs, which can be divided into liquid-like (LL), two-phase-like (TPL), and gas-like (GL) regions. Here, three regimes of SCW are obtained by the phase distribution method, which is also used for supercritical argon.⁷⁰ First, the SCW distribution in unconstrained space was simulated by MD. Periodic boundary conditions are used in all three directions. The system size is $L_x = L_y = L_z = L$, where L is the box size, depending on the SCW density at different pressures. The simulated temperature is 660 K, and the pressure is 1.0–4.0 P_c ($P_c = 22.064$ MPa), where P_c is the critical pressure of water. The number of water molecules is 2048, which was also used by Karalis *et al.*⁷¹ They indicated that using 2048 molecules can save computational resources and accurately describe the SCW properties. A relaxation of 1 ns is used to reach the equilibrium state, followed by a 5 ns run for molecule marking.

The molecule marking technique^{70,72,73} is used to identify the liquid and gas molecules for SFs. For a target molecule, the neighbor molecule number (N) in the spherical space with a neighbor radius ($r = 1.5\sigma$) is considered. The target molecule is marked as a gas molecule if $N < 5$; otherwise, the target molecule is marked as a liquid molecule. Here, the oxygen atom in the water molecule is the target atom, and the spherical neighbor radius $r = 1.5\sigma_O = 0.474$ nm. All the water molecules were marked as liquid or gas molecules. A gas mass quality ($n_{\text{gas}} = N_{\text{gas}}/N_t$) of SFs was proposed by Xu *et al.*,⁷⁰ where N_{gas} and N_t are the number of gas particles and the total number of molecules, respectively. Considering the subcritical gas–liquid two-phase states, the SFs are considered as LL, TPL, and GL phases if $n_{\text{gas}} < 0.1$, $0.1 < n_{\text{gas}} < 0.9$, and $n_{\text{gas}} > 0.9$, respectively. Figure 3 shows the density boundaries of the LL, TPL, and GL regions. SCW is considered to be in LL, TPL, and GL phases if $\rho > 534.2$, $148.5 < \rho < 534.2$, and $\rho < 148.5$ kg/m³, respectively.

III. RESULTS AND DISCUSSION

A. Variation of velocity distribution with pressure

The Poiseuille flow of water in graphene nanochannels under three surface wettability ($\theta_c = 50^\circ$, 80° , and 110°) is simulated under

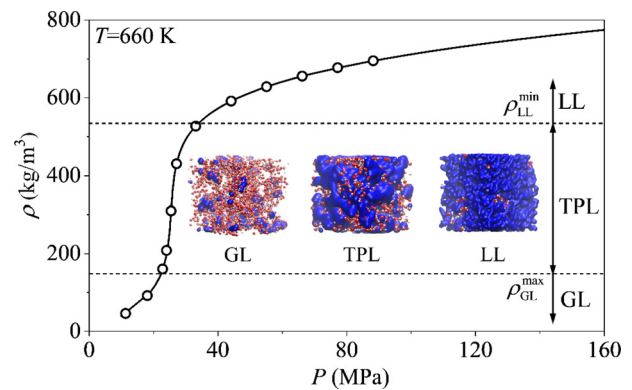


FIG. 3. Three-regime-model (GL, TPL, and LL) of SCW based on the phase distribution. The boundaries of the TPL region are $\rho_{\text{GL}}^{\text{max}} = 148.5$ and $\rho_{\text{LL}}^{\text{min}} = 534.2$ kg/m³.

$T = 660$ K and $P = 8\text{--}180$ MPa. In this range, water transitions from the gas phase to the supercritical GL, TPL, and LL phases. Figure 4 shows the velocity distribution of water along the flow direction under different wettability. As pressure increases, the velocity distribution first increases and then decreases. Thus, the velocity distribution is divided into two regions: monotonically increasing and decreasing regions. For the gas phase and GL SCW under low pressures, the velocity distribution gradually increases with pressure. For LL SCW under high pressures, the velocity distribution decreases with increasing pressure. For TPL SCW under medium pressures, the velocity distribution reaches a maximum. In addition, the average velocity under weak wettability is significantly higher than that under strong wettability,¹⁶ and the velocity distribution of LL SCW significantly changes with pressure [see Fig. 4(c)].

The density distribution of water under different wettability and pressures is further analyzed due to the correlation between the

velocity and density distributions. The density distribution is plotted in Fig. 5, corresponding to the velocity distribution pattern. The density gradually increases with pressure. The peak density of the first fluid layer (FFL) in the near-wall region gradually increases with wettability.¹⁶ Furthermore, the density distribution in the central region of the channel (1–4 nm) is inhomogeneous in the region of the monotonic increase in velocity with pressure (before the maximum value of the velocity distribution). In contrast, the density distribution in the central region of the channel is more uniform in the region after the maximum value of the velocity distribution. In addition, the fluid density in the central region of the channel corresponding to the maximum value of the velocity distribution is ~ 500 kg/m³. Thus, a correlation exists between the variation of the velocity distribution with pressure and the density distribution in the central region of the nanochannel.

To explain the velocity distribution with pressure, the variation trend of the interaction force between fluid molecules with pressure is

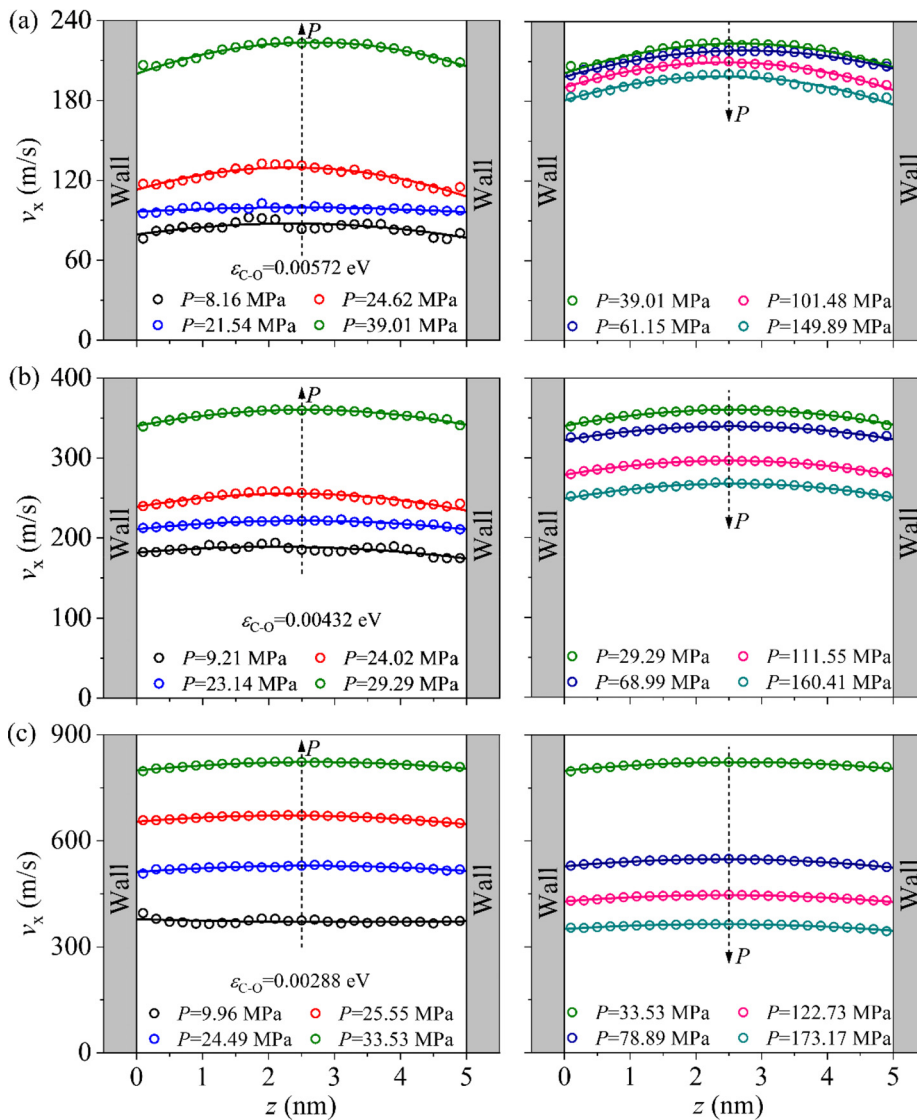


FIG. 4. The velocity distribution under different pressures and surface wettability: (a) strong wettability with $\theta_c = 50^\circ$ at $\epsilon_{c-o} = 0.00572$ eV, (b) medium wettability with $\theta_c = 80^\circ$ at $\epsilon_{c-o} = 0.00432$ eV, and (c) weak wettability with $\theta_c = 110^\circ$ at $\epsilon_{c-o} = 0.00288$ eV.

04 November 2024 09:30:57

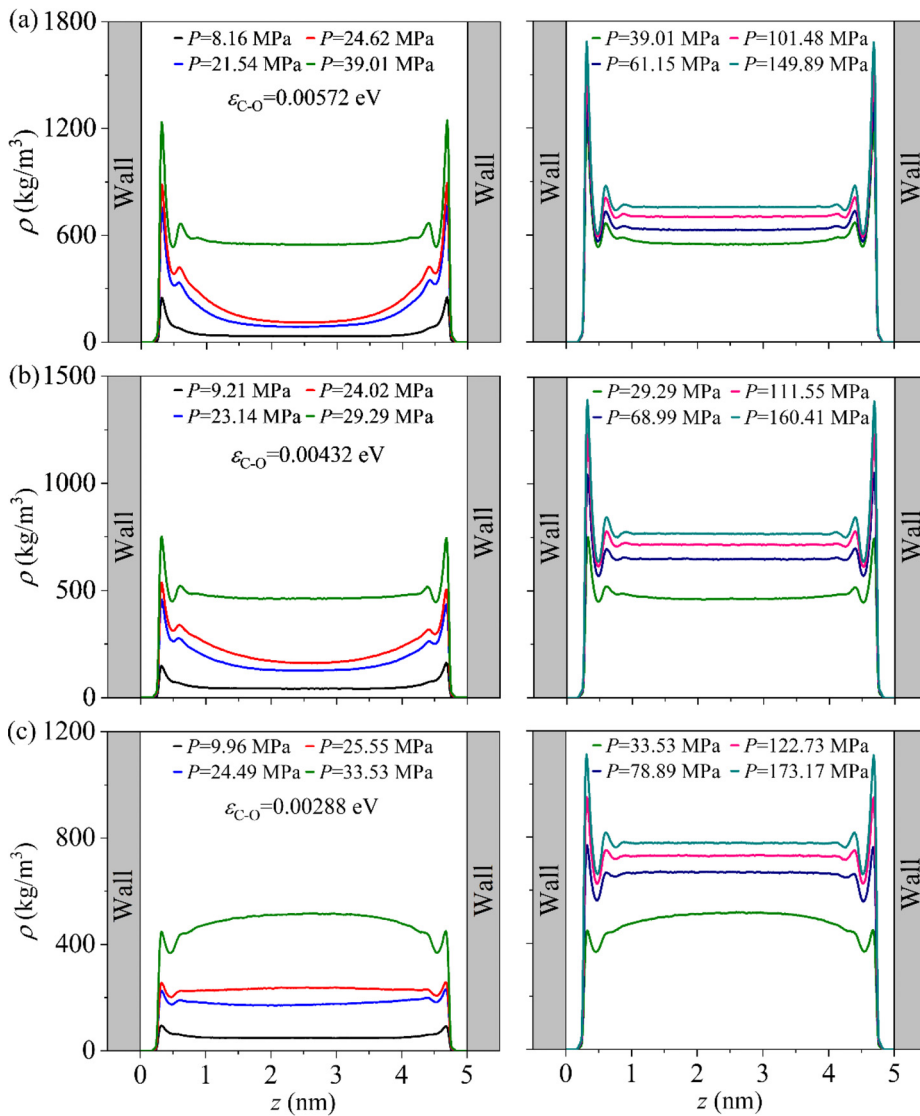


FIG. 5. The density distribution under different pressures and surface wettability: (a) strong wettability with $\theta_c = 50^\circ$ at $\epsilon_{C-O} = 0.00572$ eV, (b) medium wettability with $\theta_c = 80^\circ$ at $\epsilon_{C-O} = 0.00432$ eV, and (c) weak wettability with $\theta_c = 110^\circ$ at $\epsilon_{C-O} = 0.00288$ eV.

analyzed. For model simplification, the Coulombic interaction is neglected, and only the LJ interaction between oxygen atoms in water molecules is considered. Figure 6(a) shows the variation curve of the intermolecular interaction force of water with distance (r). As pressure increases, the fluid density increases, and the intermolecular distance decreases. The intermolecular interaction exhibits attractive forces when the distance $r > 1.12$, and repulsive forces when the distance $r < 1.12$. For the attractive dominant region, the attractive force first increases and then decreases with decreasing distance, and reaches a maximum value at $r = 1.24$.

For the Poiseuille flow simulated by MD, a constant driving force is applied in the flow direction. When the flow (velocity distribution) reaches stability, the fluid in the bulk region is in equilibrium and the total force is almost zero. This result was also obtained by Shan *et al.*⁷⁴ in their study on non-equilibrium flow in nanochannels. The force analysis in this study begins with the application of the driving force

and continues until the flow becomes stable, which is the period from force non-equilibrium to equilibrium. When a constant driving force is applied, a net force is exerted on the fluid molecules in the flow direction. The force gradually decreases with time. After a steady flow forms, the force is almost zero. During this period, the fluid molecules interact with other fluid molecules, and the intermolecular interaction force varies with the distance between them.

The analysis is based on the effect of the intermolecular interaction force on the total force of fluid molecules. Instead of considering the forces between two fluid molecules, the overall force on fluids is evaluated. The force from the solid wall atoms is neglected, a fluid molecule is subjected to the LJ forces from surrounding fluid molecules and driving force. The driving force is kept constant in the simulation. As pressure increases, the distance between fluid molecules gradually decreases. In the attractive force dominant region, the intermolecular attractive force first increases and then decreases, and hence, the total

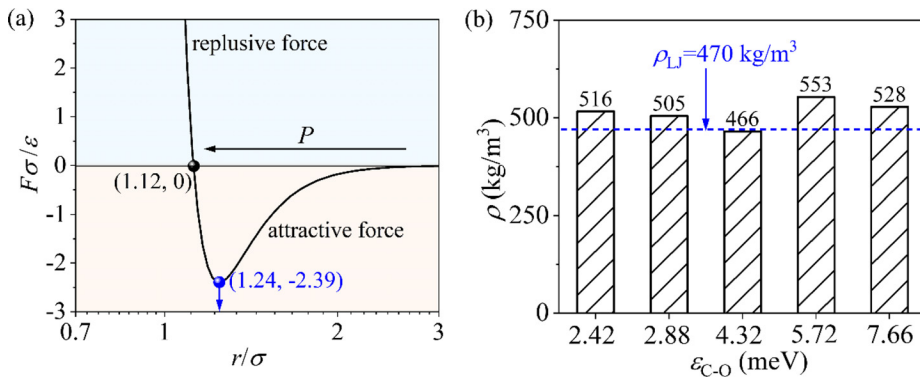


FIG. 6. Relationship between transition points of the velocity distribution and intermolecular forces with pressure: (a) the LJ interaction force vs distance and (b) comparison of the transition points of the velocity distribution under different surface wettability and the prediction based on LJ forces.

force also exhibits a similar trend. In the repulsive force dominant region, the repulsive force gradually increases; hence, the total force shows a decreasing trend. Thus, as the pressure increases, the total force first increases and then decreases, and the acceleration (a) also maintains a similar trend due to the Newton equation ($a = F/m$). Assuming that after the same time the fluid molecules are in force equilibrium and the steady-state Poiseuille flow is formed, the acceleration and velocity are positively correlated. Therefore, as the pressure increases, the velocity distribution first increases and then decreases, and the transition point occurs at the maximum value ($r = 1.24\sigma$) of the attractive force dominant region.

The above analysis shows that the variation of the fluid pressure (intermolecular forces) leads to a nonmonotonic variation of the velocity distribution. Here, the SCW density corresponding to the maximum value of the attractive force dominant region is calculated. Assuming that the distance between every two fluid molecules is d_f , the number density of fluid per unit volume is $3/\pi d_f^3$. For water molecules, $d_f = 1.24\sigma_O = 0.392$ nm, corresponding to the density value of 470 kg/m³. Figure 6(b) shows the fluid density in the central region corresponding to the transition point of the velocity distribution under different wettability. The fluid density at the transition point is around 470 kg/m³. The results verify that the variation of fluid velocity distribution with pressure is closely related to the density distribution. The nonmonotonic variation of the velocity distribution stems from the nonmonotonic variation of the intermolecular interaction force with pressure.

B. Variation of slip length with pressure

Before analyzing the variation of the slip length with pressure, the result of water-graphene Poiseuille flow at subcritical pressure is verified. The slip length under 300 K and 0.1 MPa conditions is 72.6 nm, which is consistent with the results of Celebi *et al.*,⁴⁵ indicating the reliability of the simulation results. Figure 7(a) shows the variation of the slip length with pressure under different wettability. The slip length gradually decreases with increasing wettability under similar pressure, which is consistent with the literature.^{35,38} For all wettability, the slip length first decreases, then increases, and finally decreases with increasing pressure. The variation region of the slip length with pressure is further divided in Fig. 7(b). For low-pressure (low-density) gas and GL SCW, the slip length gradually decreases with increasing pressure. For medium-pressure (medium-density) TPL SCW, the slip length increases with pressure. For high-pressure (high-density) LL SCW, the slip length

decreases with increasing pressure. In addition, the variation of the slip length with pressure gradually decreases with increasing wettability, which is in accordance with the results of Barrat and Bocquet.³⁸ Figure 7 shows that the region of monotonically increasing slip length with pressure (positive correlation, $L_s \sim P$) appears within the TPL phase, and its extent is related to surface wettability. The positive correlation region gradually decreases with the wettability. The transition point of the positive correlation region corresponds to the maximum value of the velocity distribution (see Fig. 4).

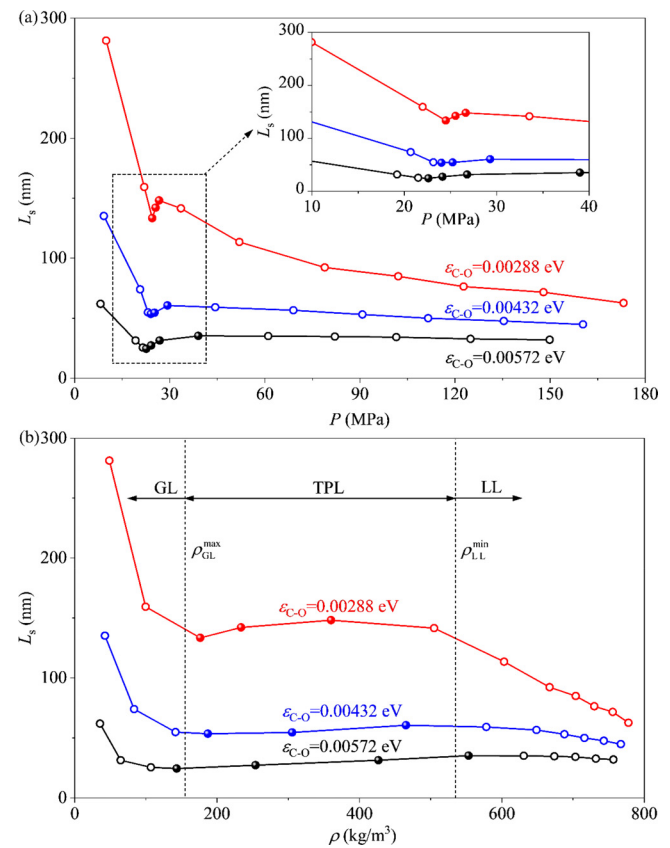


FIG. 7. Slip length (L_s) under different pressures and surface wettability: (a) L_s vs fluid pressure (P) and (b) L_s vs fluid density (ρ).

04 November 2024 09:30:57

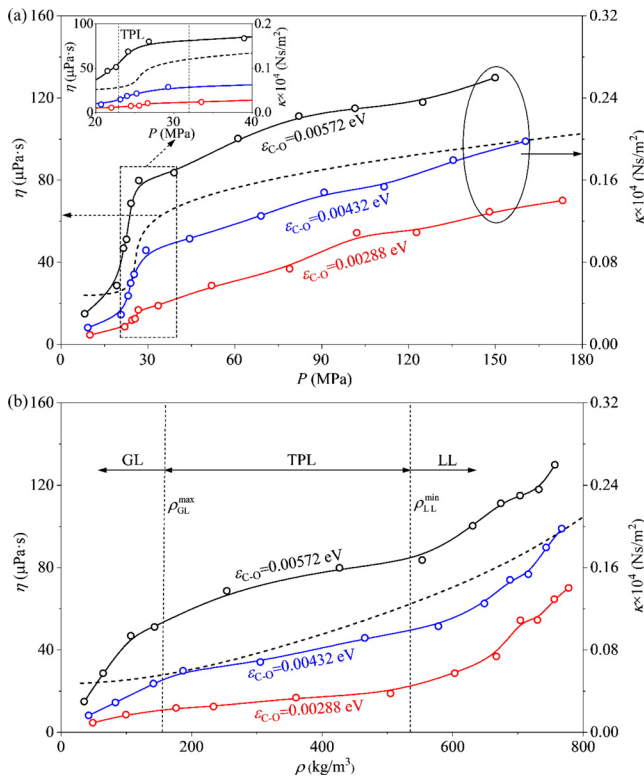


FIG. 8. Viscosity (η) and interfacial friction coefficient (κ) under different pressures and surface wettability: (a) η and κ vs fluid pressure (P) and (b) η and κ vs fluid density (ρ).

The above nonmonotonic variation of the slip length with pressure is analyzed from the perspective of the influence of pressure on properties of SFs. The slip length can be expressed as the ratio of shear viscosity (η) and friction coefficient (κ), $L_s = \eta/\kappa$.^{75,76} η can be obtained from the NIST database, and κ can be calculated by Eq. (9). Figure 8(a) shows the curves of η and κ with pressure. Both η and κ increase with pressure and surface wettability. The η - P and κ - P curves are divided into three regions. In the gas and GL regions, η slowly increases with pressure, while κ increases more quickly than η , so the slip length gradually decreases. In the TPL region, η sharply increases

with pressure,⁷⁷ and the increase in κ is lower than that of η , so the slip length increases with pressure. Under stronger wettability, the variation of κ is faster, which leads to the decrease in the positive correlation region ($L_s \sim P$), consistent with the variation of the slip length with pressure in Fig. 7(a). In the LL regions, the variation of η and κ is similar to that in the GL region. Figure 9 shows the variation of the η/κ ratio with the slip pressure and density. The variation of η/κ is consistent with the slip length shown in Fig. 7, which further validates the above analysis. Shan *et al.* proposed a similar explanation about the variation of η/κ based on the molecular kinetic theory.³⁶ In summary, the nonlinear variation of both η and κ with pressure leads to the non-monotonic variation of the slip length.

The above described variation of the slip length with pressure for SCW on the graphene surface can be divided into three regions. The slip length gradually decreases with pressure for the gas phase and GL SCW, increases for TPL SCW, and decreases for LL SCW. Compared to the result of Liang and Koblinski³⁵ and Shan *et al.*,³⁶ the slip length of supercritical argon on the graphene surface first decreased and then increased with pressure, and the minimum value occurs at the critical pressure or medium density ($\rho = 425 \text{ kg}/\text{m}^3$). Nan *et al.*³⁷ reported that the slip length of supercritical methane on the graphene surface exhibits two different variation trends depending on the fluid temperature: monotonic and nonmonotonic. At 300 and 350 K, the slip length gradually decreases and then slightly increases. While at 400 and 450 K, the slip length monotonically decreases. According to the results of this study, the slip length decreases with increasing pressure in the GL and LL regions and increases with pressure in the TPL region. The literature data are extracted and divided according to the three-regime-model,⁷⁰ which is obtained from Sec. II D. According to Liang and Koblinski,³⁵ the slip length of supercritical argon decreases with increasing pressure in GL the region, and the slip length increases with pressure in the TPL region. Similarly, Shan *et al.*³⁶ obtained the slip length minimum close to the boundary between the GL and TPL regions and observed that the slip length increases with pressure in the TPL region. Nan *et al.*³⁷ observed that at 300 and 350 K, the boundary of the GL and TPL regions is located at ~ 35 and ~ 50 MPa, respectively. The pressure range (5–60 MPa) contains the TPL region; hence, the slip length first decreases and then increases. When the temperature exceeds 400 K, the boundary of the GL and TPL regions is higher than 70 MPa. The TPL region is not present within the pressure range (5–60 MPa), so the slip length monotonically decreases with increasing pressure. The results demonstrate that the variation of the slip length

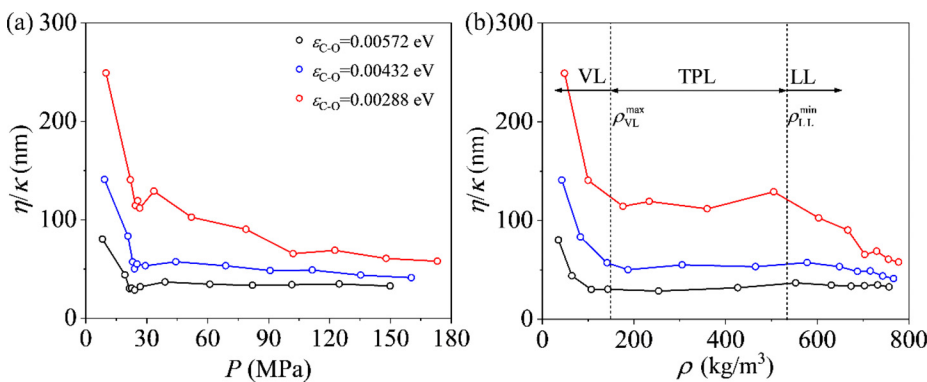


FIG. 9. The variation of the ratio of viscosity and interfacial friction coefficient under different pressures and surface wettability: (a) η/κ vs P and (b) η/κ vs ρ .

with pressure can be divided into three regions according to the phase of SFs, which is applicable to different fluid types (LJ fluid, methane, and water).

C. Microscopic mechanism for the effect of pressure on slip length

In Sec. III B, the variation of the slip length with pressure is analyzed based on the nonlinear variation trend of viscosity and interfacial friction. Here, the relationship between the interfacial friction and the slip length is explored from a microscopic perspective. The friction coefficient in Eq. (9) obtained from the Green–Kubo relationship can be rewritten as^{78,79}

$$\kappa = \frac{\tau_F}{Ak_B T} \langle F^2 \rangle, \quad (10)$$

$$\tau_F = \frac{\int_0^\infty \langle F(t)F(0) \rangle dt}{\langle F^2 \rangle}, \quad (11)$$

where τ_F is the decorrelation time for the decay of the force–force correlation function. Assuming that the main contribution of the friction force stems from the FFL, the root mean square force per unit area $\langle F^2 \rangle/A$ can be approximated as⁷⁸

$$\frac{\langle F^2 \rangle}{A} = \rho_1 S(q) (q_0 \Delta E)^2, \quad (12)$$

where ρ_1 is the fluid density in the FFL, which can be written as n_{first}/A , n_{first} is the number of fluid molecules in the FFL, A is the

cross-sectional area, ΔE is the energy barrier, and $S(q)$ is the two-dimensional structure factor, which characterizes the orderliness of the fluid structure in the FFL. A larger $S(q)$ represents a more ordered structure arrangement,⁸⁰

$$S(q) = \frac{1}{n_{\text{first}}} \left| \sum_{j=1}^N e^{i\mathbf{q} \cdot \mathbf{r}_j} \right|^2, \quad (13)$$

where n_{first} is the number of fluid molecules in the FFL, \mathbf{r}_j is the vector coordinate of the fluid molecule, and \mathbf{q} is the reciprocal lattice vector parallel to the wall. For graphene walls, $q = q_0 (1/\sqrt{3}; \pm 1)$, where q_0 is the reciprocal lattice, $q_0 = 2\pi/\sqrt{3}a_{C-C}$, and a_{C-C} is the carbon–carbon bond length.

Furthermore, ΔE is usually calculated with the position of the density peak of the FFL. However, for low-density SFs and weak wettability surfaces, the peak of the FFL is not obvious. Here, the average energy barrier ($\overline{\Delta E}$) is used to accurately characterize the energy barrier of all the fluid molecules in the FFL, and it can be calculated as follows:¹⁶

$$\overline{\Delta E} = \frac{\sum_{i=1}^n \rho_i \Delta E_i}{\sum_{i=1}^n \rho_i}, \quad (14)$$

where n is the total number of slices along the z -direction in the FFL, ρ_i is the fluid density of the i th slice parallel to the wall, and ΔE_i is the energy barrier of the i th slice. ΔE_i represents the difference between the maximum and minimum values of the potential energy field formed by the solid wall at the i th slice. Figure 10(a) shows the relationship between κ and $\langle F^2 \rangle/A$. For the same wettability, κ is

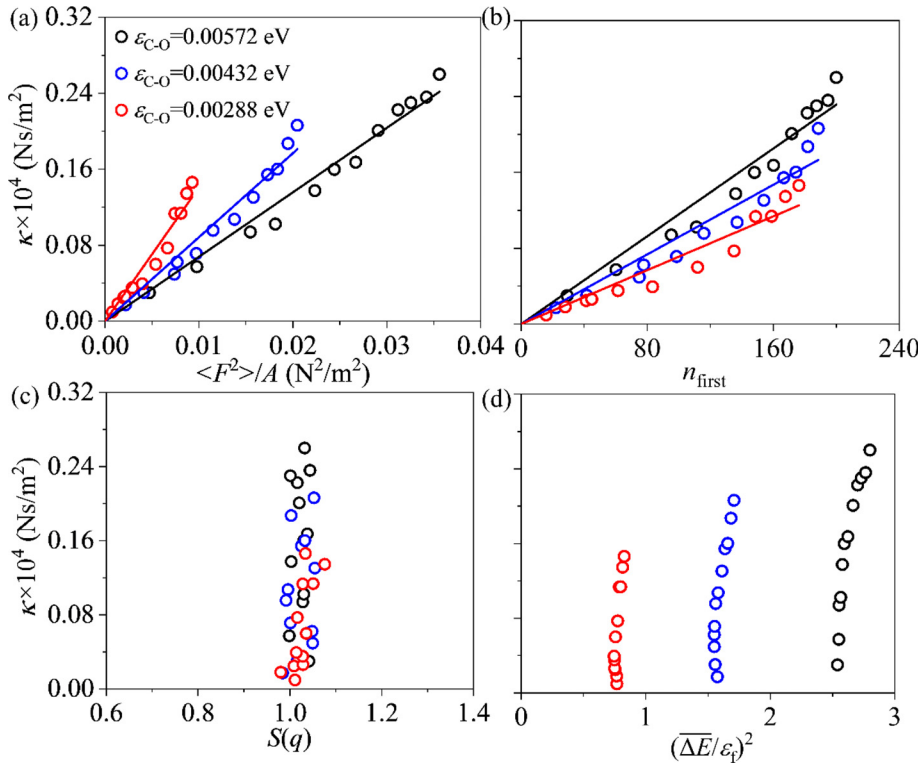


FIG. 10. Relationship between the friction coefficient (κ) and its factor: (a) κ vs root mean square force per unit area ($\langle F^2 \rangle/A$), (b) κ vs the number of fluid molecules in the FFL (n_{first}), (c) κ vs structure factor [$S(q)$], and (d) κ vs energy barrier [$(\overline{\Delta E}/\varepsilon_t)^2$].

proportional to $\langle F^2 \rangle / A$ with a slope of $\tau_F / k_B T$. As the wettability increases, the slope decreases. Thus, $\langle F^2 \rangle / A$ is mainly determined by n_{first} , $S(q)$ and ΔE in the FFL.

Figure 10(b) shows that κ is approximately proportional to n_{first} . n_{first} increases with both pressure and wettability, indicating increased friction force. The variations in pressure and wettability do not significantly affect $S(q)$. Since κ is nearly perpendicular to $S(q)$ [see Fig. 10(c)], it is insensitive to $S(q)$. For $\overline{\Delta E} / \varepsilon_f$ [see Fig. 10(d)], the enhancement of wettability significantly increases $\overline{\Delta E} / \varepsilon_f$. However, pressure has a slight effect on $\overline{\Delta E} / \varepsilon_f$ under the same wettability, so κ is insensitive to $\overline{\Delta E} / \varepsilon_f$. In summary, for the same wettability, κ is insensitive to $S(q)$ and $\overline{\Delta E} / \varepsilon_f$ and is mainly dominated by n_{first} in the FFL. For the same pressure, κ is hardly affected by $S(q)$ and is sensitive to τ_F , n_{first} and $\overline{\Delta E} / \varepsilon_f$.

The variation of the influencing factors (n_{first} and $\overline{\Delta E} / \varepsilon_f$) with pressure is analyzed. Since n_{first} cannot be directly obtained from the density distribution curve, the first peak density (ρ_f) of the FFL is used instead of n_{first} . Figure 11(a) shows that ρ_f linearly varies with n_{first} , indicating that using ρ_f instead of n_{first} is reasonable. Figure 11(b) shows ρ_f increases with pressure for all wettability. ρ_f sharply varies within the TPL region, which is consistent with the dramatic variation of density for TPL SFs. Considering the difference of density in the three regions of SCW, the density ratio (ρ_f / ρ_a) parameter is proposed, where ρ_a is the average density of the fluid in the central region of the channel. Figure 11(c) shows that ρ_f / ρ_a first significantly decreases and then slowly increases with increasing pressure. A transition point occurs approximately near the boundary between the TPL and LL regions. Therefore, for GL and TPL SCW, ρ_f / ρ_a decreases with increasing pressure, and for LL SCW, ρ_f / ρ_a increases with pressure. In addition, the enhanced wettability also leads to an increase in ρ_f / ρ_a for the

same pressure. The enhanced wettability significantly increases $\overline{\Delta E} / \varepsilon_f$ [see Fig. 11(d)]. The effect of wettability is more significant than pressure, but for LL SCW, $\overline{\Delta E} / \varepsilon_f$ slowly increases with pressure.

From Eqs. (10)–(12) and $L_s = \eta / \kappa$, the relationship between the slip length and κ , and its influencing factors [τ_F , ρ_f / ρ_a , $S(q)$, and $\overline{\Delta E} / \varepsilon_f$] are analyzed. η increases with pressure and density at the same temperature. Figure 8 shows that the slope of the η - P or η - ρ curves for LL SCW varies very little. Hence, it can be assumed that $\eta = C_1 \rho_a$, where C_1 is a constant. Therefore, L_s can be expressed as

$$L_s = \frac{Ak_B TC_1 \rho_{\text{ave}}}{\tau_F \langle F^2 \rangle} \sim \frac{Ak_B TC_1}{\tau_F (n_{\text{first}} / \rho_a) S(q) (q_0 \overline{\Delta E})^2} \sim \frac{1}{\tau_F (\rho_f / \rho_a) S(q) (\overline{\Delta E} / \varepsilon_f)^2}, \quad (15)$$

where $Ak_B TC_1$ is a constant. L_s is determined by τ_F , ρ_f / ρ_a , $S(q)$, and $\overline{\Delta E}$. $S(q)$ is insensitive to pressure and wettability [see Fig. 10(c)]. Therefore, for LL SCW, L_s is determined by τ_F , ρ_f / ρ_a , and $\overline{\Delta E}$. Figure 12(a) shows the relationship between L_s and $1 / ((\rho_f / \rho_a) (\overline{\Delta E} / \varepsilon_f)^2 \tau_F)$ for LL SCW, and Eq. (15) is verified. Figures 12(b)–12(d) show the relationship between L_s and a single factor (ρ_f / ρ_a and $\overline{\Delta E} / \varepsilon_f$). For the same wettability, L_s is linearly correlated with $1 / (\rho_f / \rho_a)$, and $1 / (\overline{\Delta E} / \varepsilon_f)^2$. However, under all wettability conditions, L_s is only linearly correlated with ρ_f / ρ_a . The result stems from the change of τ_F under different wettability. Thus, L_s can be evaluated using two parameters ρ_f / ρ_a and $\overline{\Delta E} / \varepsilon_f$. The $L_s \sim 1 / (\rho_f / \rho_a)$ relationship is applicable for the LL region.

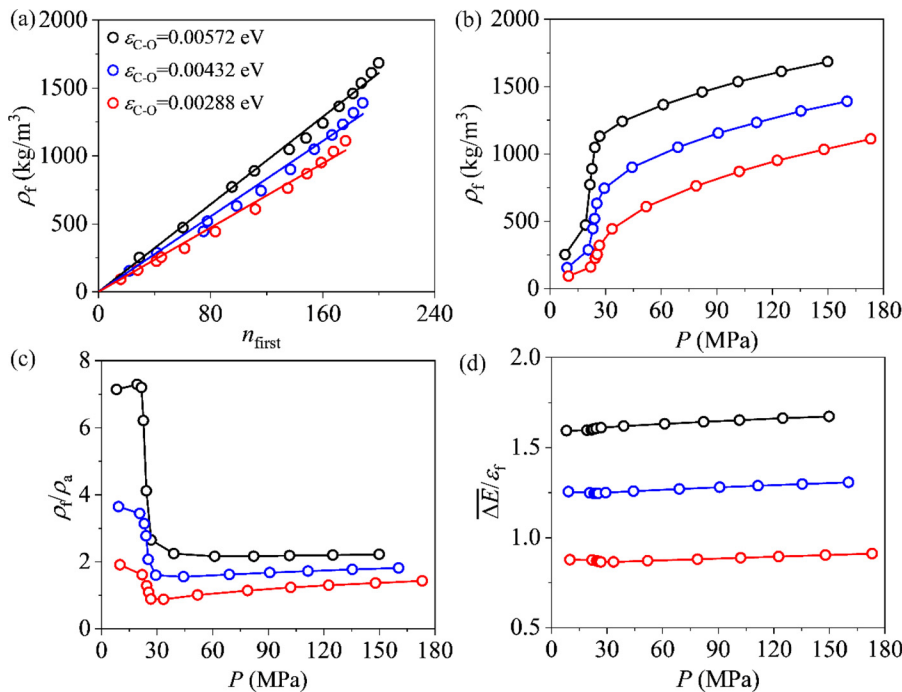


FIG. 11. Factors of friction coefficient with pressure: (a) ρ_f vs n_{first} , (b) ρ_f vs P , (c) ρ_f / ρ_a vs P , and (d) $\overline{\Delta E} / \varepsilon_f$ vs P .

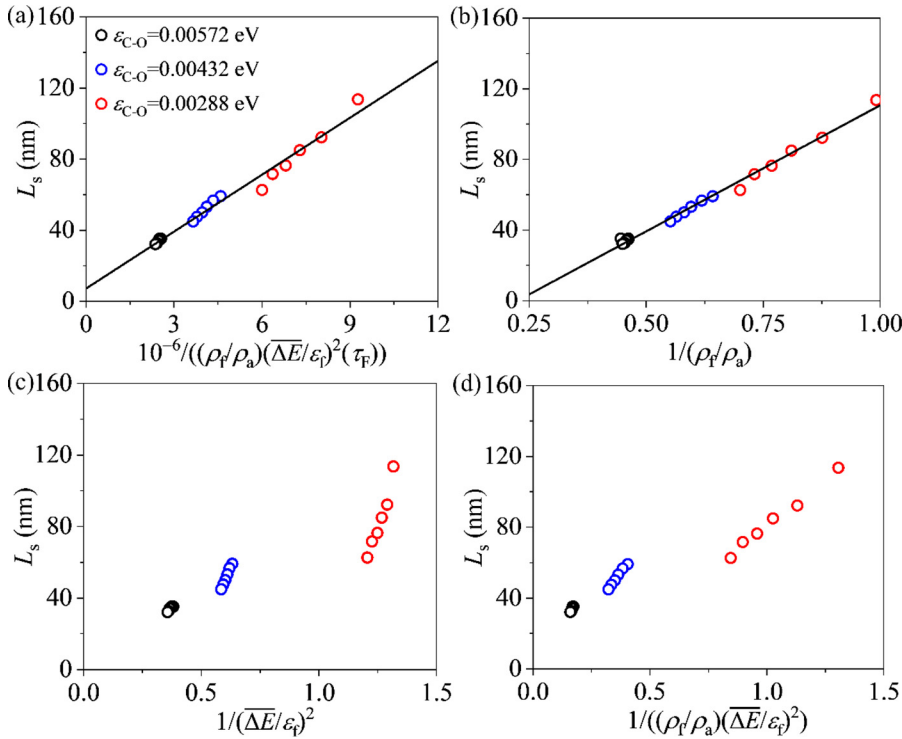


FIG. 12. Relationship between the slip length for LL SCW and factors: (a) L_s vs $1/((\rho_{first}/\rho_{ave})(\overline{\Delta E}/\epsilon_f)^2\tau_F)$, (b) L_s vs $1/(\rho_f/\rho_a)$, (c) L_s vs $1/(\overline{\Delta E}/\epsilon_f)^2$, and (d) L_s vs $1/(\rho_f/\rho_a)(\overline{\Delta E}/\epsilon_f)^2$.

For the gas phase, GL, and TPL SWC, the mechanism of the effect of pressure on the slip length is further explored. Figure 13 shows that L_s is negatively correlated with pressure in the gas and GL regions, i.e., $L_s \sim 1/P$. For subcritical gas, L_s can be calculated according to the Maxwell first-order slip model. The classical Maxwell slip model is applicable to dilute gases. Here, due to the similarity between the subcritical gas phase and the low-density supercritical GL phase, the applicability of the slip model is extended. The Maxwell slip model is used to determine the slip length for GL SCW,^{81,82}

$$L_s = \lambda \frac{2 - \sigma_t}{\sigma_t}, \tag{16}$$

$$\lambda = \frac{k_B T}{\sqrt{2} \pi d^2 P}, \tag{17}$$

where σ_t is the tangential momentum coefficient, representing the proportion of molecules reflected by diffusion from the solid wall, λ is the mean free path, and d is the effective diameter of molecules, which is ~ 0.4 nm for water. As the pressure increases, the gas adsorption on the wall surface increases, which increases σ_t . λ decreases with increasing pressure due to the increase in fluid density. Therefore, for low-density gas and GL, L_s decreases with increasing pressure. For gas flow, the Knudsen number ($Kn = \lambda/H$) is used to describe the no-slip and slip boundary conditions. As pressure increases, Kn is in the range of 0.1068–0.2265 for gas and GL SCW, which is in the slip and transient regions ($0.001 < Kn < 1$). Therefore, it is reasonable to analyze L_s for gas and GL SCW by Eq. (16). The Maxwell slip model can still qualitatively reflect the variation of the slip length with pressure. A similar analysis has been conducted in the literature.³⁵

In the TPL region, L_s first increases with pressure and then decreases close to the LL region. The range of the positive correlation region between L_s and pressure is related to surface wettability. To simplify the analysis, only the positive correlation between L_s and pressure ($L_s \sim P$) for the TPL region is considered herein. Section III B explains that the positive correlation between L_s and pressure in the TPL region is based on the variation of viscosity and interfacial friction with pressure. Figure 13 shows the relationship between L_s and ρ_f/ρ_a in the TPL region. For the same wettability, L_s is approximately negatively correlated with ρ_f/ρ_a , which is similar to the results in the LL region. However, the slope of $L_s \sim \rho_f/\rho_a$ under different wettability varies,

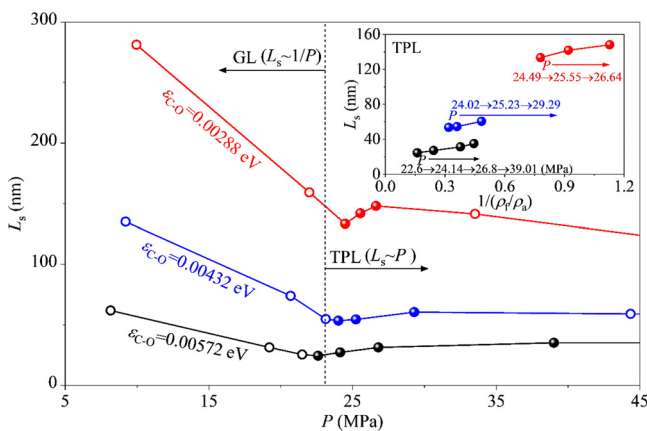


FIG. 13. Variation of the slip length with pressure for GL and TPL SCW.

which is different from the result for the LL region. Therefore, for TPL SCW, the parameter ρ_l/ρ_a can still reflect the trend of L_s to some extent.

D. Verification of the effect of pressure on slip length

The variation of the slip length with pressure under different wettability is analyzed in Secs. III B and III C, and here, additional strong hydrophilic ($\theta_c = 10^\circ$, $\epsilon_{C-O} = 0.00766$ eV) and hydrophobic cases ($\theta_c = 120^\circ$, $\epsilon_{C-O} = 0.00242$ eV) are analyzed to verify the results under a wide range of wettability. Figure 14 shows that the variation of the slip length with pressure under all wettability can be divided into three regions. In addition, the transition of the positive correlation region ($L_s \sim P$) shifts toward low pressure as wettability decreases, which is consistent with the previous analysis (see Fig. 7). The $L_s \sim \rho_l/\rho_a$ relationship is satisfied for strong wettability ($\epsilon_{C-O} = 0.00766$ eV), while for the weak wettability ($\epsilon_{C-O} = 0.00242$ eV), the slope of $L_s \sim \rho_l/\rho_a$ curve increases. This is because of the weak fluid–solid interaction, which leads to the fluid density distribution near the wall no longer having a density peak. The previous analysis of interfacial friction mainly considered the effect of the FFL. However, due to the blurring or even disappearance of the FFL,¹⁶ the fluid density distribution closer to the central region needs to be considered to calculate the interfacial friction.

In addition to wettability, the relationship between the slip length and pressure is also verified for different channel heights. The $L_s \sim P$ curve exhibits a similar variation trend under channel heights of 5 and 8 nm (see Fig. 15), and the $L_s \sim \rho_l/\rho_a$ relationship is still satisfied. However, the L_s of LL SCW at 8 nm slightly increases compared to that at 5 nm. For subcritical fluids, the relationship between L_s and channel height has been extensively studied. If the channel height is small, the Poiseuille flow obtained by non-equilibrium molecular dynamics methods generates noise that affects the calculation of L_s .²⁴ L_s is independent of the channel height when the height exceeds the threshold. For the water–graphene system under subcritical conditions ($T = 300$ K), L_s does not significantly vary when the channel height exceeds 5 nm.²⁴ For the water–graphene system under supercritical conditions ($T = 660$ K) in this paper, L_s at 8 nm is slightly larger than that at 5 nm, which may be because of the increase in velocity due to

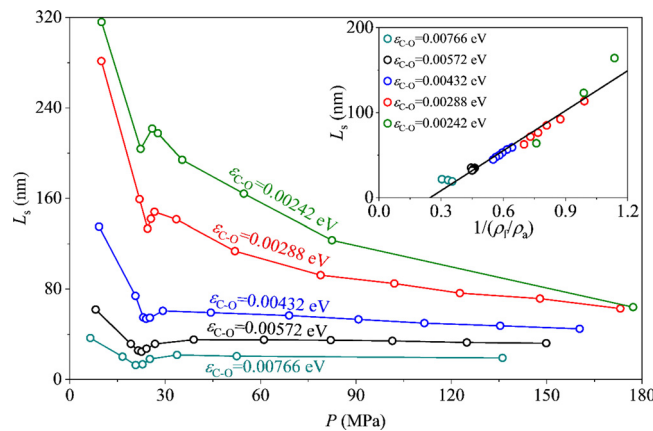


FIG. 14. Variation of the slip length with pressure under a wide range of surface wettability.

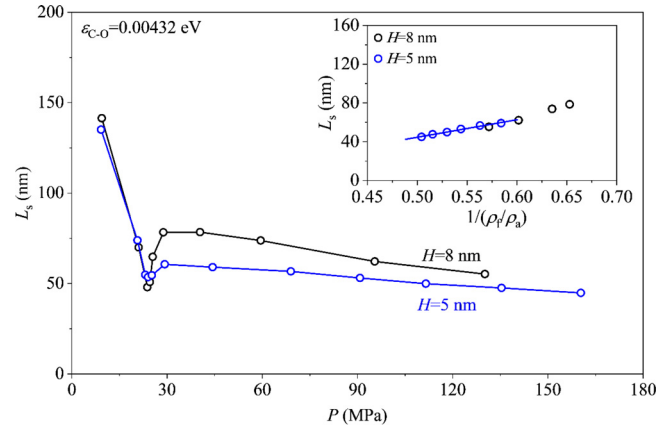


FIG. 15. Variation of the slip length with pressure under different channel heights ($H = 5$ and 8 nm).

the violent thermal motion of fluid molecules at high temperatures. The relationship between L_s and channel height for SFs needs to be further investigated.

For the flow of LJ fluids on solid surfaces with FCC lattice, L_s monotonically decreases with increasing pressure under weak wettability and is almost constant under strong wettability.^{35,38} The effect of the wall types on the slip length is considered, and a typical copper surface with FCC lattice is selected. The slip length on the copper surface is significantly reduced compared to that on the graphene surface.³⁵ To analyze the variation of the slip length with pressure, weak wettability ($\theta_c = 170^\circ$, $\epsilon_{Cu-O} = 0.00155$ eV) is considered. Figure 16(a) shows that the velocity distribution of SCW on copper nanochannels first increases and then decreases with increasing pressure, which is consistent with the observations for graphene nanochannels. Similarly, the slip length on the copper surface nonmonotonically varies with pressure [see Fig. 16(c)], which can be divided into three regions. In contrast to the results of Barrat and Bocquet,³⁸ who observed that L_s monotonically decreases with increasing pressure, L_s increases with pressure in the TPL region in this study. Two reasons exist for this difference. First, the range of the TPL region is small, and only one or two data points are selected, which does not reflect the overall variation. Second, for solids with FCC lattice, L_s significantly decreases compared to that for graphene, and the small magnitude variation of L_s in the TPL region is insignificant under moderate and strong wall wettability. In addition, for the LL region, the $L_s \sim \rho_l/\rho_a$ relationship is still satisfied [see Fig. 16(c)]. The relationship between the slip length and pressure is the same for different solid wall types, such as graphene and metallic copper walls.

IV. CONCLUSIONS

Flow transport of SFs in nanochannels is widespread in shale and hot dry rock reservoirs. Understanding the slip behavior under supercritical conditions is essential for improving the efficiency of supercritical systems. Pressure and surface wettability are the main factors affecting the interfacial slip. In this study, the Poiseuille flow of SCW in graphene and copper nanochannels was simulated through MD, and the effect of pressure on the slip length under different surface

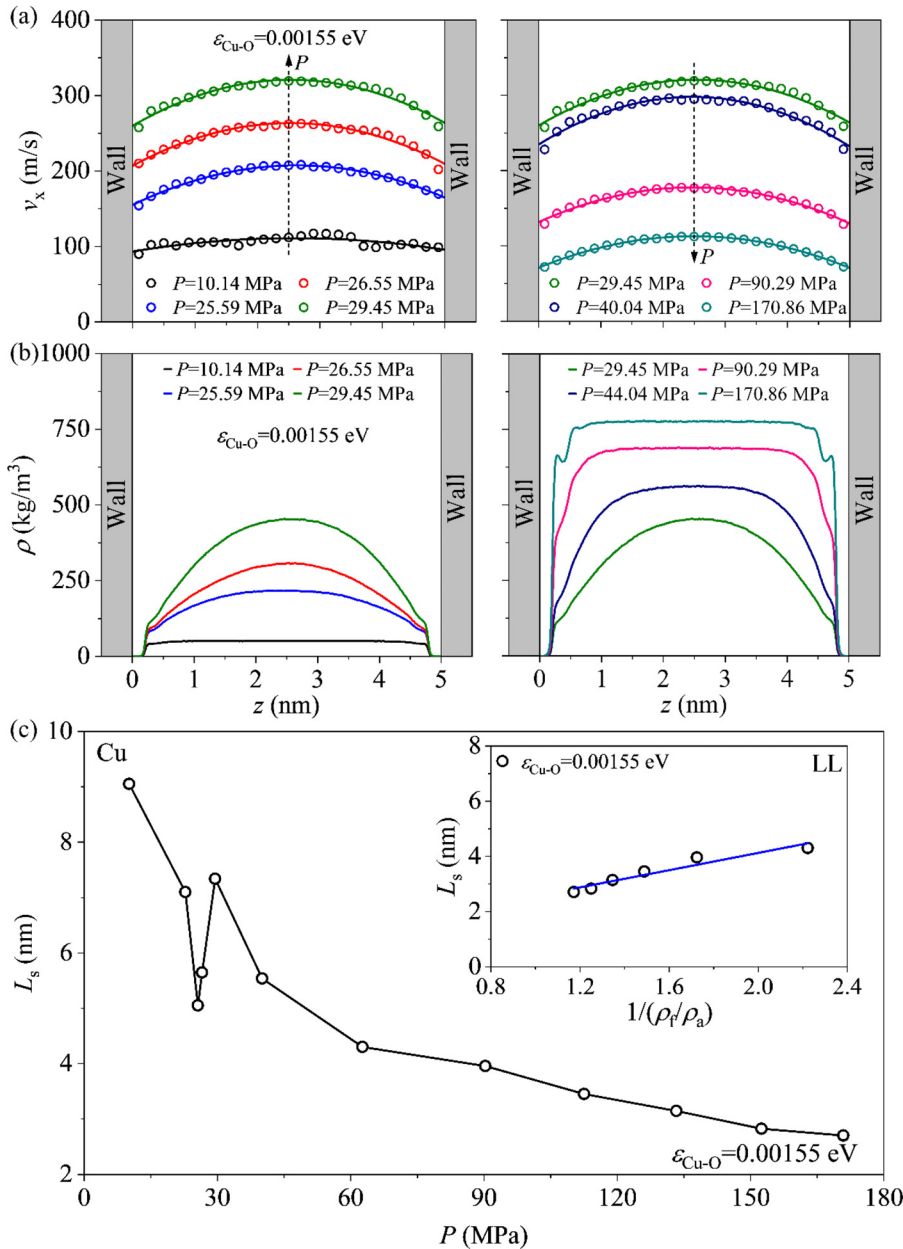


FIG. 16. Flow and slip behaviors in copper nanochannels under weak surface wettability ($\theta_c = 170^\circ$ at $\epsilon_{Cu-O} = 0.00155$ eV): (a) density distribution with pressure, (b) velocity distribution with pressure, and (c) variation of the slip length with pressure.

wettability was investigated. The conclusions are summarized as follows:

1. As pressure increases, with the phase transition from the gas phase to supercritical GL, TPL, and LL phases at the same temperature, the velocity distribution first increases and then decreases. Such velocity distribution stems from the nonmonotonic variation of the intermolecular interaction force with pressure.
2. The variation of slip length with pressure is divided into three regions. For the gas phase and GL SCW, the slip length gradually

decreases with increasing pressure. For TPL SCW, the slip length increases with pressure. For LL SCW, the slip length decreases with increasing pressure. The slip length nonmonotonically varies with the pressure due to the nonlinear variation of the fluid viscosity and interfacial friction with pressure.

3. For the gas phase and GL SCW, the Maxwell slip model effectively describes the negative correlation between the slip length and pressure ($L_s \sim 1/P$). For LL SCW, the microscopic mechanism of the effect of pressure on the slip length is revealed from the interfacial friction perspective. The slip length is evaluated based on two parameters: density ratio and energy barrier. The

results show that the $L_s \sim 1/(\rho_l/\rho_a)$ relationship can describe the variation of slip length with pressure for all wettability. For TPL SCW, such a relationship only describes the variation of slip length for the same wettability.

- The relationship between the slip length and pressure is applicable to a wide range of wettability, different channel heights, different fluid types (LJ fluid, methane, and water), and different solid wall types (graphene and copper).

ACKNOWLEDGMENTS

This work was supported by the Natural Science Foundation of China (Nos. 52130608 and 51821004).

AUTHOR DECLARATIONS

Conflict of Interest

The authors have no conflicts to disclose.

Author Contributions

Ming Dong: Investigation (equal); Software (equal); Visualization (equal); Writing – original draft (equal). **Jinliang Xu:** Funding acquisition (lead); Resources (lead); Writing – review & editing (lead). **Yan Wang:** Investigation (equal); Software (equal); Visualization (equal).

DATA AVAILABILITY

The data that support the findings of this study are available from the corresponding author upon reasonable request.

REFERENCES

- Q. Wang and R. Li, “Research status of shale gas: A review,” *Renewable Sustainable Energy Rev.* **74**, 715 (2017).
- R. S. Middleton, R. Gupta, J. D. Hyman, and H. S. Viswanathan, “The shale gas revolution: Barriers, sustainability, and emerging opportunities,” *Appl. Energy* **199**, 88 (2017).
- T. Reinsch, P. Dobson, H. Asanuma, E. Huenges, F. Poletto, and B. Sanjuan, “Utilizing supercritical geothermal systems: A review of past ventures and ongoing research activities,” *Geotherm. Energy* **5**, 16 (2017).
- F. Parisio, V. Vilarrosa, W. Wang, O. Kolditz, and T. Nagel, “The risks of long-term re-injection in supercritical geothermal systems,” *Nat. Commun.* **10**, 4391 (2019).
- S. Rani, E. Padmanabhan, and B. K. Prusty, “Review of gas adsorption in shales for enhanced methane recovery and CO₂ storage,” *J. Pet. Sci. Eng.* **175**, 634 (2019).
- A. Fatah, H. B. Mahmud, Z. Bennour, R. Gholami, and M. Hossain, “The impact of supercritical CO₂ on the pore structure and storage capacity of shales,” *J. Nat. Gas Sci. Eng.* **98**, 104394 (2022).
- J. B. Curtis, “Fractured shale-gas systems,” *AAPG Bull.* **86**, 1921 (2002).
- H. Wang, L. Chen, Z. Qu, Y. Yin, Q. Kang, B. Yu, and W. Q. Tao, “Modeling of multi-scale transport phenomena in shale gas production—A critical review,” *Appl. Energy* **262**, 114575 (2020).
- H. Yu, H. Xu, J. Fan, Y.-B. Zhu, F. Wang, and H. Wu, “Transport of shale gas in microporous/nanoporous media: Molecular to pore-scale simulations,” *Energy Fuels* **35**, 911 (2021).
- W. Sparreboom, A. van den Berg, and J. C. Eijkel, “Principles and applications of nanofluidic transport,” *Nat. Nanotechnol.* **4**, 713 (2009).
- P. Bampoulis, K. Sotthewes, E. Dollekamp, and B. Poelsema, “Water confined in two-dimensions: Fundamentals and applications,” *Surf. Sci. Rep.* **73**, 233 (2018).
- H. Zhu, Y. Wang, Y. Fan, J. Xu, and C. Yang, “Structure and transport properties of water and hydrated ions in nano-confined channels,” *Adv. Theor. Simul.* **2**, 1900016 (2019).
- L. Bocquet and J. L. Barrat, “Flow boundary conditions from nano- to micro-scales,” *Soft Matter* **3**, 685 (2007).
- D. C. Tretheway and C. D. Meinhart, “Apparent fluid slip at hydrophobic microchannel walls,” *Phys. Fluids* **14**, L9 (2002).
- M. Chinappi and C. M. Casciola, “Intrinsic slip on hydrophobic self-assembled monolayer coatings,” *Phys. Fluids* **22**, 042003 (2010).
- H. Hu, L. Bao, N. V. Priezjev, and K. Luo, “Identifying two regimes of slip of simple fluids over smooth surfaces with weak and strong wall-fluid interaction energies,” *J. Chem. Phys.* **146**, 034701 (2017).
- M. A. Samaha and M. Gad-el-Hak, “Slippery surfaces: A decade of progress,” *Phys. Fluids* **33**, 071301 (2021).
- K. Kobayashi, K. Aoki, H. Tabe, H. Fujii, T. Nara, H. Takashima, N. Oshima, and M. Watanabe, “Couette flow at high Knudsen number between wall and liquid boundaries,” *Phys. Fluids* **35**, 082021 (2023).
- H. Yang, B. Zeng, X. Zhang, Y. Xing, X. Gui, and Y. Cao, “Control of boundary slip by interfacial nanobubbles: A perspective from molecular dynamics simulations,” *Phys. Fluids* **35**, 032108 (2023).
- X. Yong and L. T. Zhang, “Slip in nanoscale shear flow: Mechanisms of interfacial friction,” *Microfluid. Nanofluid.* **14**, 299 (2013).
- N. V. Priezjev and S. M. Troian, “Influence of periodic wall roughness on the slip behaviour at liquid/solid interfaces: Molecular-scale simulations versus continuum predictions,” *J. Fluid Mech.* **554**, 25 (2006).
- B. Y. Cao, M. Chen, and Z. Y. Guo, “Liquid flow in surface-nanostructured channels studied by molecular dynamics simulation,” *Phys. Rev. E* **74**, 066311 (2006).
- J. Xu and Y. Li, “Boundary conditions at the solid-liquid surface over the multi-scale channel size from nanometer to micron,” *Int. J. Heat Mass Transfer* **50**, 2571 (2007).
- B. Ramos-Alvarado, S. Kumar, and G. P. Peterson, “Hydrodynamic slip length as a surface property,” *Phys. Rev. E* **93**, 023101 (2016).
- J. Ghorbanian and A. Beskok, “Scale effects in nano-channel liquid flows,” *Microfluid. Nanofluid.* **20**, 121 (2016).
- S. Zhan, Y. Su, M. Lu, M. Cai, J. Fu, Z. Liu, K. Wang, and Q. Han, “Effect of surface type on the flow characteristics in shale nanopores,” *Geofluids* **2021**, 6641922.
- B. Shan, R. Wang, Z. Guo, and P. Wang, “Contribution quantification of nano-scale gas transport in shale based on strongly inhomogeneous kinetic model,” *Energy* **228**, 120545 (2021).
- S. Wang, F. Javadpour, and Q. Feng, “Fast mass transport of oil and supercritical carbon dioxide through organic nanopores in shale,” *Fuel* **181**, 741 (2016).
- J. He, Y. Ju, K. Kulasinski, L. Zheng, and L. Lammers, “Molecular dynamics simulation of methane transport in confined organic nanopores with high relative roughness,” *J. Nat. Gas Sci. Eng.* **62**, 202 (2019).
- P. Huang, L. Shen, F. Maggi, Z. Chen, and Z. Pan, “Influence of surface roughness on methane flow in shale kerogen nano-slits,” *J. Nat. Gas Sci. Eng.* **103**, 104650 (2022).
- A. Sidorenkov, M. Stukan, and V. Ivanov, “Methane flow in nanopores: Analytical approximation based on MD simulations,” *Fuel* **332**, 126070 (2023).
- B. Liu, C. Qi, X. Zhao, G. Teng, L. Zhao, H. Zheng, K. Zhan, and J. Shi, “Nanoscale two-phase flow of methane and water in shale inorganic matrix,” *J. Phys. Chem. C* **122**, 26671 (2018).
- S. Wang, Q. Feng, M. Zha, F. Javadpour, and Q. Hu, “Supercritical methane diffusion in shale nanopores: Effects of pressure, mineral types, and moisture content,” *Energy Fuels* **32**, 169 (2018).
- L. Zhang, Q. Li, C. Liu, Y. Liu, S. Cai, S. Wang, and Q. Cheng, “Molecular insight of flow property for gas-water mixture (CO₂/CH₄-H₂O) in shale organic matrix,” *Fuel* **288**, 119720 (2021).
- Z. Liang and P. Keblinski, “Slip length crossover on a graphene surface,” *J. Chem. Phys.* **142**, 134701 (2015).
- B. Shan, P. Wang, R. X. Wang, Y. Zhang, and Z. Guo, “Molecular kinetic modelling of nanoscale slip flow using a continuum approach,” *J. Fluid Mech.* **939**, A9 (2022).
- Y. Nan, W. Li, and Z. Jin, “Slip length of methane flow under shale reservoir conditions: Effect of pore size and pressure,” *Fuel* **259**, 116237 (2020).
- J. L. Barrat and L. Bocquet, “Large slip effect at a nonwetting fluid-solid interface,” *Phys. Rev. Lett.* **82**, 4671 (1999).

- ³⁹J. Włoch, A. P. Terzyk, and P. Kowalczyk, "New forcefield for water nanodrop-let on a graphene surface," *Chem. Phys. Lett.* **674**, 98 (2017).
- ⁴⁰J. L. F. Abascal and C. Vega, "A general purpose model for the condensed phases of water: TIP4P/2005," *J. Chem. Phys.* **123**, 234505 (2005).
- ⁴¹D. Corradini, M. Rovere, and P. Gallo, "The Widom line and dynamical cross-over in supercritical water: Popular water models versus experiments," *J. Chem. Phys.* **143**, 114502 (2015).
- ⁴²L. Lindsay and D. A. Broido, "Optimized Tersoff and Brenner empirical potential parameters for lattice dynamics and phonon thermal transport in carbon nanotubes and graphene," *Phys. Rev. B* **81**, 205441 (2010).
- ⁴³M. Shen, P. K. Schelling, and P. Keblinski, "Heat transfer mechanism across few-layer graphene by molecular dynamics," *Phys. Rev. B* **88**, 045444 (2013).
- ⁴⁴M. Sega, M. Sbragaglia, L. Biferale, and S. Succi, "Regularization of the slip length divergence in water nanoflows by inhomogeneities at the Angstrom scale," *Soft Matter* **9**, 8526 (2013).
- ⁴⁵A. T. Celebi, C. T. Nguyen, R. Hartkamp, and A. Beskok, "The role of water models on the prediction of slip length of water in graphene nanochannels," *J. Chem. Phys.* **151**, 174705 (2019).
- ⁴⁶T. Werder, J. H. Walther, R. Jaffe, T. Halicioglu, and P. Koumoutsakos, "On the water-carbon interaction for use in molecular dynamics simulations of graphite and carbon nanotubes," *J. Phys. Chem. B* **107**, 1345 (2003).
- ⁴⁷D. C. Rapoport, *The Art of Molecular Dynamics Simulation* (Cambridge University Press, 2004).
- ⁴⁸F. Li, I. A. Korotkin, and S. A. Karabasov, "Rheology of water flows confined between multilayer graphene walls," *Langmuir* **36**, 5633 (2020).
- ⁴⁹I. C. Yeh and M. L. Berkowitz, "Ewald summation for systems with slab geometry," *J. Chem. Phys.* **111**, 3155 (1999).
- ⁵⁰J. P. Ryckaert, G. Ciccotti, and H. J. Berendsen, "Numerical integration of the Cartesian equations of motion of a system with constraints: Molecular dynamics of *n*-alkanes," *J. Comput. Phys.* **23**, 327 (1977).
- ⁵¹W. G. Hoover, "Canonical dynamics: Equilibrium phase-space distributions," *Phys. Rev. A* **31**, 1695 (1985).
- ⁵²E. Wagemann, E. Oyarzua, J. H. Walther, and H. A. Zambrano, "Slip divergence of water flow in graphene nanochannels: The role of chirality," *Phys. Chem. Chem. Phys.* **19**, 8646 (2017).
- ⁵³S. Bernardi, B. Todd, and D. J. Searles, "Thermostating highly confined fluids," *J. Chem. Phys.* **132**, 244706 (2010).
- ⁵⁴X. Yong and L. T. Zhang, "Thermostats and thermostat strategies for molecular dynamics simulations of nanofluidics," *J. Chem. Phys.* **138**, 084503 (2013).
- ⁵⁵S. Plimpton, "Fast parallel algorithms for short-range molecular dynamics," *J. Comput. Phys.* **117**, 1–19 (1995).
- ⁵⁶R. Raj, S. C. Maroo, and E. N. Wang, "Wettability of graphene," *Nano Lett.* **13**, 1509 (2013).
- ⁵⁷I. Morcos, "On contact angle and dispersion energy of the cleavage graphite/water system," *J. Colloid Interface Sci.* **34**, 469 (1970).
- ⁵⁸Z. Li, Y. Wang, A. Kozbial, G. Shenoy, F. Zhou, R. McGinley, P. Ireland, B. Morganstein, A. Kunkel, S. P. Surwade *et al.*, "Effect of airborne contaminants on the wettability of supported graphene and graphite," *Nat. Mater.* **12**, 925 (2013).
- ⁵⁹S. Wang, Y. Zhang, N. Abidi, and L. Cabrales, "Wettability and surface free energy of graphene films," *Langmuir* **25**, 11078 (2009).
- ⁶⁰F. Taherian, V. Marcon, N. F. van der Vegt, and F. Leroy, "What is the contact angle of water on graphene?," *Langmuir* **29**, 1457 (2013).
- ⁶¹D. Parobek and H. Liu, "Wettability of graphene," *2D Mater.* **2**, 032001 (2015).
- ⁶²J. Feng and Z. Guo, "Wettability of graphene: From influencing factors and reversible conversions to potential applications," *Nanoscale Horiz.* **4**, 339 (2019).
- ⁶³L. A. Belyaeva and G. F. Schneider, "Wettability of graphene," *Surf. Sci. Rep.* **75**, 100482 (2020).
- ⁶⁴S. K. Kannam, B. D. Todd, J. S. Hansen, and P. J. Daivis, "Slip length of water on graphene: Limitations of non-equilibrium molecular dynamics simulations," *J. Chem. Phys.* **136**, 024705 (2012).
- ⁶⁵A. T. Celebi, M. Barisik, and A. Beskok, "Electric field controlled transport of water in graphene nano-channels," *J. Chem. Phys.* **147**, 164311 (2017).
- ⁶⁶Z. Gao, N. Giovambattista, and O. Sahin, "Phase diagram of water confined by graphene," *Sci. Rep.* **8**, 6228 (2018).
- ⁶⁷M. Barisik and A. Beskok, "Equilibrium molecular dynamics studies on nanoscale-confined fluids," *Microfluid. Nanofluid.* **11**, 269 (2011).
- ⁶⁸A. Pham, M. Barisik, and B. Kim, "Pressure dependence of Kapitza resistance at gold/water and silicon/water interfaces," *J. Chem. Phys.* **139**, 244702 (2013).
- ⁶⁹A. P. Thompson, S. J. Plimpton, and W. Mattson, "General formulation of pressure and stress tensor for arbitrary many-body interaction potentials under periodic boundary conditions," *J. Chem. Phys.* **131**, 154107 (2009).
- ⁷⁰J. Xu, Y. Wang, and X. Ma, "Phase distribution including a bubblelike region in supercritical fluid," *Phys. Rev. E* **104**, 014142 (2021).
- ⁷¹K. Karalis, C. Ludwig, and B. Niceno, "Supercritical water anomalies in the vicinity of the Widom line," *Sci. Rep.* **9**, 15731 (2019).
- ⁷²J. Losey and R. J. Sadus, "Structural behavior of fluids from the vapor and liquid region to the supercritical phase," *Phys. Rev. E* **100**, 052132 (2019).
- ⁷³Y. Wang, J. Xu, M. Dong, J. Xie, and Q. Wang, "Phase distribution in nano-channels of supercritical fluid with different fluid-wall interactions," *Phys. Fluids* **35**, 062002 (2023).
- ⁷⁴B. Shan, L. Ju, W. Su, Z. Guo, and Y. Zhang, "Non-equilibrium flow of van der Waals fluids in nano-channels," *Phys. Fluids* **35**, 052004 (2023).
- ⁷⁵J. L. Barrat, "Influence of wetting properties on hydrodynamic boundary conditions at a fluid/solid interface," *Faraday Discuss.* **112**, 119 (1999).
- ⁷⁶L. Bocquet and J. L. Barrat, "On the Green-Kubo relationship for the liquid-solid friction coefficient," *J. Chem. Phys.* **139**, 044704 (2013).
- ⁷⁷P. Gallo, D. Corradini, and M. Rovere, "Widom line and dynamical crossovers as routes to understand supercritical water," *Nat. Commun.* **5**, 5806 (2014).
- ⁷⁸K. Falk, F. Sedlmeier, L. Joly, R. R. Netz, and L. Bocquet, "Molecular origin of fast water transport in carbon nanotube membranes: Superlubricity versus curvature dependent friction," *Nano Lett.* **10**, 4067 (2010).
- ⁷⁹W. Xiong, J. Z. Liu, M. Ma, Z. Xu, J. Sheridan, and Q. Zheng, "Strain engineering water transport in graphene nanochannels," *Phys. Rev. E* **84**, 056329 (2011).
- ⁸⁰P. A. Thompson and M. O. Robbins, "Shear flow near solids: Epitaxial order and flow boundary conditions," *Phys. Rev. A* **41**, 6830 (1990).
- ⁸¹J. C. Maxwell, "VII. On stresses in rarified gases arising from inequalities of temperature," *Philos. Trans. R. Soc. London* **170**, 231 (1879).
- ⁸²B. Y. Cao, J. Sun, M. Chen, and Z. Y. Guo, "Molecular momentum transport at fluid-solid interfaces in MEMS/NEMS: A review," *Int. J. Mol. Sci.* **10**, 4638 (2009).